Artifacts reduction in high-acutance phase images for X-ray grating interferometry

Georges Giakoumakis, Jérôme Primot, Amélie Jarnac, Laureen Guitard, Adrien Stolidi

Artifacts reduction in high-acutance phase images for X-ray grating interferometry

GEORGES GIAKOUMAKIS[1,2*], JÉRÔME PRIMOT[1], AMÉLIE JARNAC[3], LAUREEN GUITARD[1,2] AND ADRIEN STOLIDI[2]

[1] *Université Paris-Saclay, ONERA, DOTA, F-91123 Palaiseau, France*
[2] *Université Paris-Saclay, CEA, List, F-91120, Palaiseau, France*
[3] *Université Paris-Saclay, ONERA, DPHY, F-91123 Palaiseau, France*
[*] *georges.giakoumakis@onera.fr*

Abstract: X-ray grating-based techniques often lead to artifacts in the phase retrieval process of phase objects presenting very fast spatial transitions or sudden jumps, especially in the field of non-destructive testing and evaluation. In this paper, we present a method that prevents the emergence of artifacts by building an interferogram corrected from any variations of intensity of the object and given as input in the phase extraction process. For illustration, this method is applied to a carbon fiber specimen imaged by a microfocus X-ray tube and a single 2D grating. A significant reduction of artifacts has been obtained, by a factor higher than 10. This evaluation has been performed thanks to the Confidence Map tool, a recently developed method that estimates the error distribution from the data sets.

1. Introduction

One of the most used techniques to measure the phase shift of the wavefront in X-rays consists in introducing a modulator between the source and the detector that produces a reference intensity pattern. This pattern is distorted when the wavefront is aberrant, which is the case after adding a phase object into the optical path. The reference intensity pattern can be randomly or regularly distributed: speckle-based techniques [1, 2] use randomly distributed intensity pattern while grating-based techniques [3–9] use regularly distributed intensity pattern, that we call interferogram. Among the regular 2D grating based devices, multi-lateral shearing interferometers (MLSI) offer the benefit of simultaneously measuring the phase shift of the wavefront in multiple orientations [10–12]. In X-ray phase imaging using MLSI, complex phase objects with abrupt intensity transitions such as edges or splits, can be strenuous to be phase sampled by the grating. In the particular case where the transitions of the object evolve faster than the period of the interferogram, artifacts arise in the phase image. Classically, apodization technique could be performed in order to reduce artifacts however lowering the spatial resolution of the phase image [13]. Another recent approach [14] has proposed to combine several images acquired while spatially shifting the grating in an effort to reduce artifacts and enhance the spatial resolution, however this method is only applicable in the case of low-acutance phase images. Here we propose a preventive approach that reduces accurately artifacts in high-acutance phase images while keeping the spatial resolution unchanged, called MARIO for *Method of Artifacts Reduction from the Intensity of the Object*. After introducing the problems in section 2 based on simulated data, we present the formalism of this new process in section 3, and demonstrate its interest on experimental data in section 4. Since the proposed technique is somewhat cumbersome, as it requires the acquisition of an additional image, we evaluate its interest in a quantitative way by using the Confidence Map, a tool that we introduced in our previous work [15].

2. Influence of abrupt phase and attenuation transition in retrieval process: illustration using MLSI technique

Based on a wavefront approach, simulated data presented in Figure 1 (a,b) summarize the MLSI procedure. Using a monochromatic divergent point source at 17.48 keV (Mo Kα line, of wavelength $\lambda = 7.0929\ 10^{-11}$ m) with a detection plan made of 2048×2048 squared pixels of 6.5×6.5 µm^2, Figure 1 (a) presents the image of a 2D-checkerboard phase grating with orthogonal period $p = 12$ µm and a $[0 - \pi]$ shift at Mo Kα. This image is called the reference interferogram I_{ref}. The second image, I_{mod} (Figure 1 (b)) is produced with the same grating parameters in addition to a canonical object, here a ball of radius of 750 µm made of PMMA material. Finally, Figure 1 (c) presents the image of the PMMA ball I_{obj} without the grating, produced with the same object parameters. The source-detector distance is $d_{sd} = 60$ cm for a grating and object magnification factor of $G_g = 5$ and $G_o = 7$ respectively. Since the MLSI uses a periodic modulator, phase retrieval is classically performed according to the Fourier formalism and compares the phase shift between I_{ref} and I_{mod} by studying in their spectrum variations induced by the object. All corresponding Fourier transforms modulus are presented in Figure 1 (d,e,f).

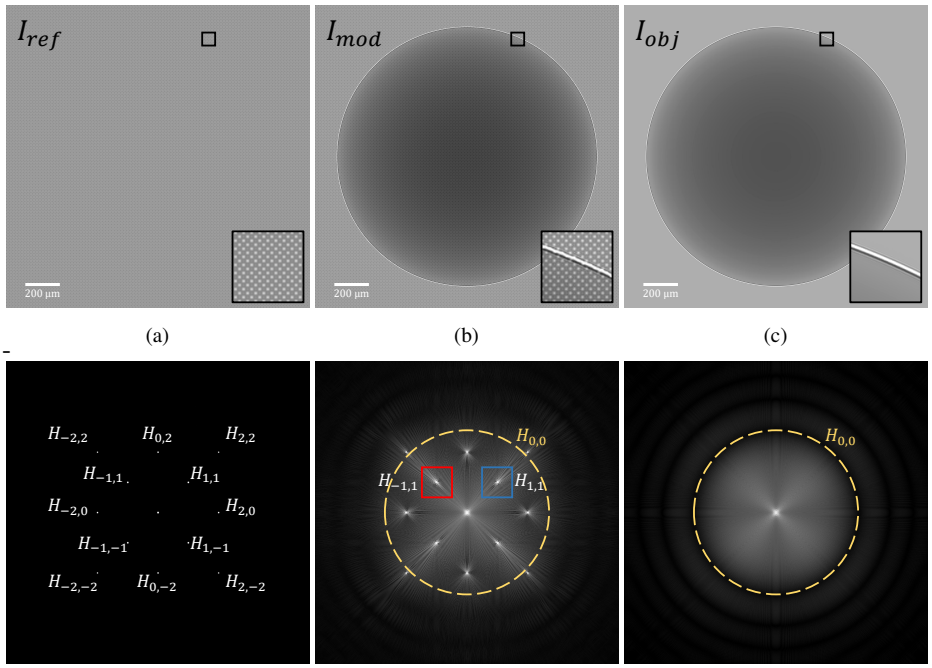

Fig. 1. (a) Simulated single grating image with (b) a PMMA ball and (c) without the grating. (d,e,f) Corresponding Fourier transform modulus. The Fourier transforms of I_{ref} (d) contains the 12 harmonics from the grating (denoted $H_{k,l}$ with $k, l \in \{0; \pm 1; \pm 2\}$). The Fourier transform of I_{obj} (f) contains a central harmonic $H_{0,0}$ holding the absorption and edge overshoot information of the PMMA ball. Its main frequency range is wide (denoted by the yellow dotted circle). The Fourier transform of I_{mod} (e) results in an overlap between the modulated $H_{k,l}$ and $H_{0,0}$. In the extraction window of $H_{-1,1}$ and $H_{1,1}$ (see red and blue square), extra frequencies from $H_{0,0}$ are taken into account.

The Fourier transform of the reference interferogram (Figure 1 (d)) contains harmonics denoted

$H_{k,l}$ with $(k,l) \in \mathbb{Z}^2$ since the signal I_{ref} is periodic along several orientations and can be decomposed into a sum of sinusoidal functions oriented along the same directions. Their expression can be retrieved by taking the auto-correlation of the diffracted orders generated by the MLSI [10]. Here, the simulated grating diffracts over 5 orders leading to 12 principal harmonics in the Fourier plan: $H_{\pm1,\pm1}$, $H_{0,\pm2}$,$H_{\pm2,0}$, $H_{\pm2,\pm2}$, carrying redundant information of the wavefront gradient. On the other hand, the Fourier transform of the PMMA ball (Figure 1 (f)) contains a central harmonic denoted $H_{0,0}$ holding the absorption and edge overshoot information of the object. The frequency extension of $H_{0,0}$ is wide in the Fourier plan (see the yellow circle) since the intensity of the PMMA ball evolves fast, especially at its edges. The Fourier transform of the modulated interferogram I_{mod} (Figure 1 (e)) thus results in a frequency overlap between $H_{0,0}$ and all modulated harmonics $H_{k,l}$ of the grating.

To retrieve the phase gradient $G_{k,l}$ (Figure 2 (a,b)), one has to perform the argument of the inverse Fourier transform of $H_{k,l}$ on an extraction window centered at the carrier frequency $f_{k,l}$ (see corresponding red and blue rectangles in Figure 1 (e)). The size of the extraction window is given by the space between two consecutive harmonics in the Fourier plan [16]. The Fourier derivative theorem is then applied to retrieve the phase image $\phi_{k,l}$ (Figure 2 (c)) from a couple of two orthogonal gradients $(G_{k,l}, G_{-l,k})$. In this example, the extraction support of the harmonics $H_{k,l}$ are composed of the true signal and the residual signal from $H_{0,0}$, denoted $Res_{H_{0,0}}$. These extra frequencies in the extraction window lead to artifacts in the gradient estimation $G_{k,l}$. Such artifacts arise in the gradients images $G_{-1,1}$, $G_{1,1}$ at the edge of the PMMA ball (Figure 2 (a,b)), materialized by phase jumps (also called phase dislocations) and affecting the final phase image (Figure 2 (c)). A similar behavior is observed for each other phase gradient measured by the MLSI.

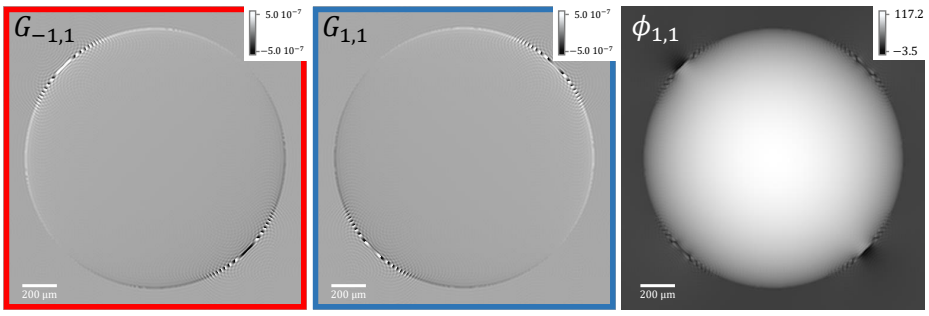

(a) (b) (c)

Fig. 2. (a) Gradient $G_{-1,1}$ and (b) gradient $G_{1,1}$ showing artifacts at the edge of the object, region where the edge intensity overshoot evolves faster than the interferogram periodicity. (c) Phase retrieved $\phi_{1,1}$ from the gradients $G_{-1,1}$ and $G_{1,1}$ showing the influence of the artifacts from $G_{-1,1}$ and $G_{1,1}$.

3. Reduction of artifacts in the phase gradients estimation

Artifacts in phase gradient images arise as soon as frequencies from two or more harmonics overlap in the Fourier plan. The major contributor to the frequency overlap is the central harmonic $H_{0,0}$ since its amplitude is the highest in X-ray imaging. Thus, we propose to build an interferogram I_{corr} that does not hold any intensity information from the sample in order to minimize the amplitude of $H_{0,0}$. This can be done simply by subtracting the modulated interferogram I_{mod} by the attenuation image of the sample I_{obj}. The new interferogram I_{corr} is built according to the following expression:

$$I_{corr}(x,y) = I_{mod}(x,y) - \alpha I_{obj}(x,y) + \beta \,, \tag{1}$$

where $\alpha \leq 1$ is a constant that normalizes the dynamics of the attenuation image I_{obj} to match the dynamics of I_{mod}, and $\beta > 0$ is a constant for readjusting the dynamics of I_{corr} around the mean gray value of the initial interferogram I_{mod}. The expression of α and β is given below :

$$\alpha = \frac{< I_{mod}(x,y) >_{\Omega}}{< I_{obj}(x,y) >_{\Omega}} , \tag{2a}$$

$$\beta = < I_{ref}(x,y) >_{\Omega} , \tag{2b}$$

where Ω refers to a same region of interest $\{x_i, y_j\}$ in each image, defined in an area outside the sample; $< \square >_{\Omega}$ corresponds to the mean gray value of a given intensity inside Ω. The new interferogram I_{corr} is then compared to the reference one I_{ref} and phase retrieval is performed conventionally. Figure 3 illustrates the construction of the new interferogram I_{corr} and the phase gradient extraction process.

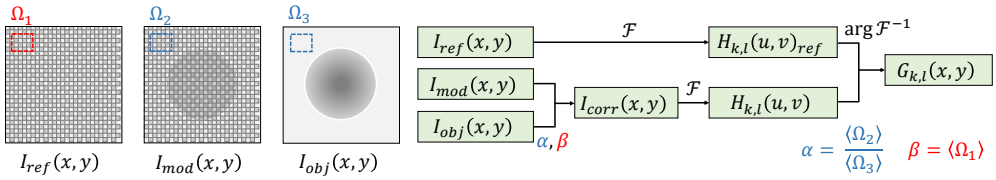

Fig. 3. Illustration of the construction of the corrected interferogram I_{corr} (see equation 1) and of the phase gradient extraction process. $\mathcal{F}$ refers to the Fourier transform and Ω_i refers to a region of interest in each image used to calculate the mean intensity value of I_{ref}, I_{mod} and I_{obj} from which α and β are derived.

Figure 4 presents the phase retrieval results after performing the proposed MARIO. Compared to the images presented in Figure 2, the amplitude of the artifacts is significantly reduced in the gradient images (Figure 4 (a,b)) leading to a better restitution of the edges of the ball in the phase image (Figure 4 (c)).

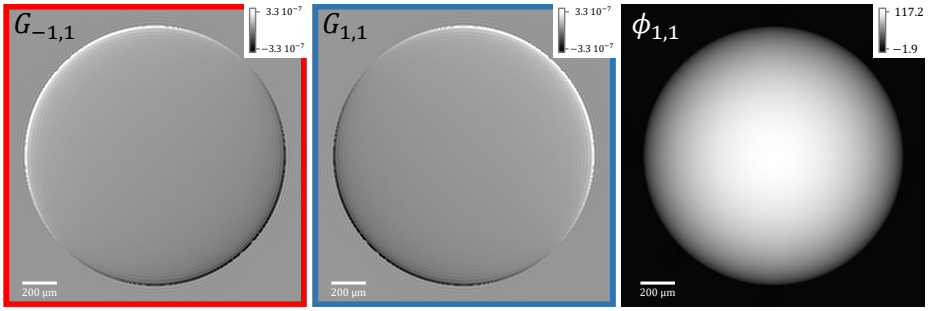

(a) (b) (c)

Fig. 4. (a) Gradient $G_{-1,1}$ and (b) gradient $G_{1,1}$ obtained after applying the proposed MARIO process. (c) Phase retrieved $\phi_{1,1}$ from the gradients $G_{-1,1}$ and $G_{1,1}$. Compared to the images shown in Figure 2, artifacts are significantly reduced.

The gain of the proposed MARIO is evaluated by comparing the retrieved phase ϕ_r and the theoretical phase ϕ_t of the same PMMA ball at 17.48 keV. The phase residual is therefore the difference at each point (x, y) between ϕ_t and ϕ_r. The Root Mean Square Error ($RMSE$) is then

performed:

$$RMSE = \frac{1}{N}\sqrt{\sum_{x=0}^{N-1}\sum_{y=0}^{N-1}\left(\phi_t(x,y) - \phi_r(x,y)\right)^2}, \tag{3}$$

where N denotes the number of points of the phase image along each axis. The $RMSE$ of the raw phase image $\phi_{1,1}$ retrieved with the raw gradients $(G_{-1,1}, G_{1,1})$ (see Figure 2) is equal to $RMSE(\phi_{1,1}) = 2.73$ πrad. After performing the proposed MARIO (see Figure 4), $RMSE(\phi_{1,1}) = 0.12$ πrad that is a reduction of the phase error by 22.0. Analogously, the $RMSE$ of the raw phase image $\phi_{2,0}$ retrieved with the raw gradients $(G_{0,2}, G_{2,0})$ (not displayed for better succinctness) is equal to $RMSE(\phi_{2,0}) = 1.84$ πrad. After performing the proposed MARIO, $RMSE(\phi_{2,0}) = 0.18$ πrad that is a gain of 10.0.

4. Application on experimental image

After demonstrating the MARIO process on a model case, we apply the method on an experimental case, the X-ray imaging of a Carbon Fiber Reinforced Polymer (CFRP). This sample, manufactured in a controlled laboratory environment as model for lightning damage experiment [17], is made of sixteen plys of aligned carbon fibers with a diameter of 12 ± 3 µm (successive plys are oriented at -45°; +45°) surrounded by Epoxy resin. This sample is particularly well adapted to highlight the influence of fast transitions on the phase retrieval process for two reasons: central holes with very steep edges and a high resolution structure linked to the weaving. The sample is imaged using the MLSI bench shown in Figure 5. It is composed of a single 2D checkerboard grating manufactured by the Microworks company. The π-phase shift of the grating is induced by Gold material of 3.49 µm thickness deposited on a polymer substrate. The X-ray source is a divergent microfocus tube (Feinfocus FXE-160.51) of a measured spot size of 5.5 µm with a solid transmitted Tungsten anode imaged by a sCMOS high resolution detector (Hamamatsu C12819-102-U) with a Gadox scintillator of thickness of 20 µm. Here, $d_{sd} = 57$ cm giving a grating magnification of $G_g = 3.3$ and an object magnification of $G_o = 2.3$. The grating orthogonal period and the pixel size of the detector remain unchanged from the simulation study.

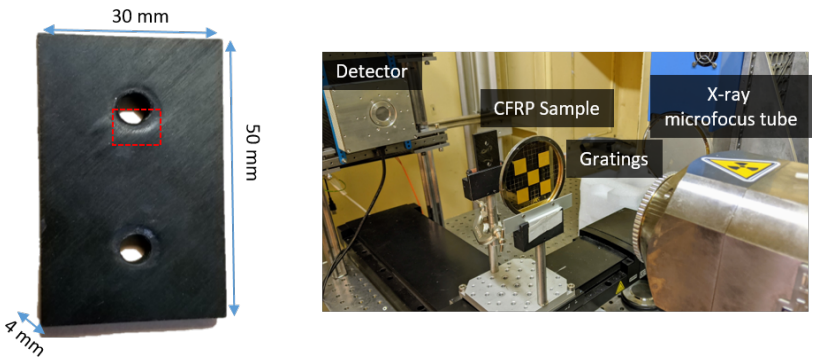

Fig. 5. CFRP sample with the imaged region denoted by the red dashed line rectangle (left). Experimental bench with a microfocus X-ray source, 2D-gratings, CFRP sample and a high-resolution detector (right).

Experimental data are presented in Figure 6, acquired in a specific area of the CFRP (spotted by the red dashed line rectangle in Figure 5). The left column (Figure 6 (a,d)) presents the image of the CFRP and its Fourier transform modulus. The distribution of the central harmonic $H_{0,0}$ in the Fourier plan reveals two regions: the first one is linked to the absorption of the carbon

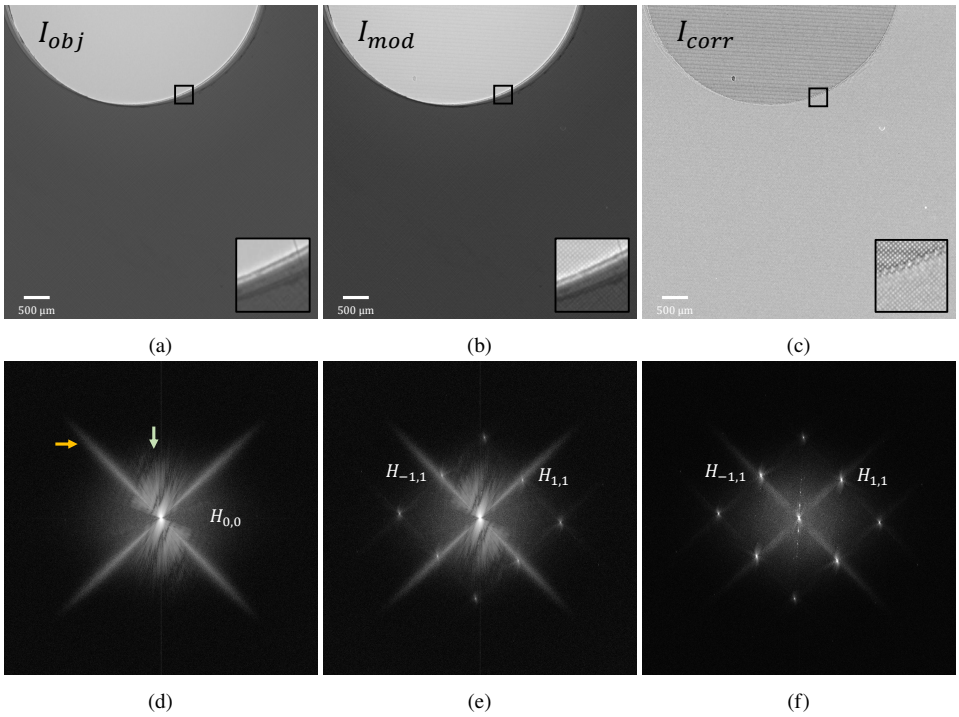

Fig. 6. (a) Raw image of the CFRP sample alone. (b) Raw image of the grating and the CFRP sample without and (c) with the application of the MARIO process. Bottom row, the corresponding Fourier transform. The green and yellow arrows in (d) relate to the spectral distribution of respectively the edge intensity overshoot and the absorption of the CFRP. This leads in (e) to a frequency overlap with the harmonics of the grating. In (f), the influence of the CFRP spectral distribution has been minimized according to the MARIO process.

fibers, oriented at -45°; +45° (see orange arrow in Figure 6 (d)). Since they induce fast intensity transitions, it results in a wide distribution in the Fourier plan. The second region (see green arrow) is linked to the edge intensity overshoot of the CFRP (see zoom box in Figure 6 (a)) and is also of wide spectral distribution.

The middle column (Figure 6 (b,e)) presents the image of the CFRP acquired after placing the grating into the optical path (see zoom box in Figure 6 (b)) and its associated Fourier transform modulus. The harmonics $H_{k,l}$ of the grating are distributed in the same way as for the simulation study. A frequency overlap between the harmonics $H_{k,l}$ and the central harmonic $H_{0,0}$ is noticeable. Moreover, the amplitude of the $H_{k,l}$ harmonics is lower than that the amplitude of $H_{0,0}$ since the fringe intensity contrast is lower than the sample intensity contrast.

The right column (Figure 6 (c,f)) presents the interferogram I_{corr} corrected by the MARIO process and its associated Fourier transform modulus. The attenuation of the sample as well as its edge intensity overshoot has been removed, highlighted by a more uniform gray level in the zoom box in Figure 6 (c). In the associated Fourier transform image, the amplitude of $H_{0,0}$ is minimized while maintaining the amplitude of all harmonics $H_{k,l}$ unaffected. It should also be noted that subtracting the intensity of the object in the interferogram does not enhance the fringes contrast in the areas where the attenuation of the object is the highest, keeping the phase measurement more sensitive to the noise in these regions.

The corrected interferogram I_{corr} is then given as an input in the phase retrieval process.

Experimental results are presented in Figure 7, without (top row) and with (bottom row) the MARIO process. Since the harmonics $H_{-1,1}$ and $H_{1,1}$ have the highest signal-to-noise ratio in the Fourier plan, they are used to display the phase gradients $G_{-1,1}$ and $G_{1,1}$. In the raw phase gradients images (Figure 7 (a,b)), artifacts arise at the edges of the hole (see green arrows). Moreover, artifacts from the oriented carbon fibers (-45°; +45°) arise throughout the sample, evolving in the direction of the measured gradient (see orange arrows in Figure 7 (a,b)). In the phase image (Figure 7 (c)), these artifacts induce a textured aspect of the sample where slowly evolving gray level variations give a mottled appearance. In the gradients images processed by MARIO (Figure 7 (d,e)), edge artifacts as well as carbon fibers artifacts are significantly reduced, cleaning the phase image from nearly all dislocations (Figure 7 (f)).

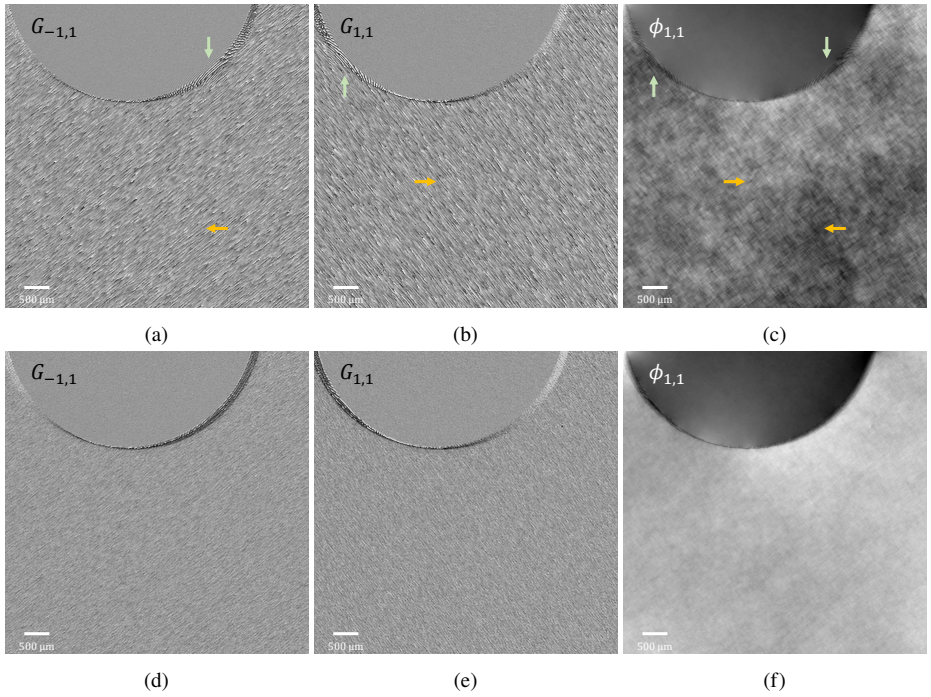

Fig. 7. Top row, uncorrected experimental results: (a) gradient $G_{-1,1}$ and (b) gradient $G_{1,1}$. (c) Phase image $\phi_{1,1}$ retrieved from the gradients in (a,b). The green arrows point the edge artifacts while the orange arrows point the artifacts in the object. Bottom row: corresponding corrected images by the MARIO process. All artifacts are significantly reduced in the gradients and phase images.

The gain of the proposed MARIO on experimental data is evaluated by performing the Confidence Map [15]. This method gives an estimation of the experimental errors for any phase image retrieved by a gradient-based device, taking advantage of the fact that the MLSI measures at least two orthogonal gradients simultaneously. So, it is possible to calculate a phase derivative closure map by applying the curl operator. As we assume that the wavefront issued from the sample is a continuous surface, the value of the phase derivative closure map should be equal to zero in all points. However in real conditions, this calculation is different from zero and suffer from several errors contributions: noise ϵ_n, under-sampling ϵ_u or dislocations ϵ_d. By analyzing the histogram of the phase derivative closure map, each error type is assigned a threshold value. The Confidence Map is built and colors the error pixels according to their type. For instance, phase dislocations are displayed with red pixels, under-sampling errors with blue pixels and noise with cyan pixels. Therefore, the Confidence Map alerts the observer of the presence of

artifacts that could affect his interpretation of the image. Figure 8 (a) presents the Confidence Map of the CFRP raw phase image superimposed to the phase image (see Figure 7 (c)). ϵ_d alerts are displayed here in red, ϵ_u in blue, and ϵ_n are not displayed for better visualization. These results are the same as the ones presented in our previous work [15]. Figure 8 (b) presents the Confidence Map of the CFRP phase image after performing MARIO process; a clear reduction of the phase dislocation alerts ϵ_d as well as the under-sampling alerts ϵ_u are observed inside and at the edge of the sample. For better visualization, a short footage is given as supplemental materials. The percentage of dislocation alerts over the phase image, defined as the ratio between the red pixel amount and the total pixel amount of the image, is equal to $\epsilon_d = 3.2\%$ before any treatment. This ratio decreases to 0.2% after the applying the MARIO process. In the meantime, the percentage of under-sampling alerts decreases from $\epsilon_u = 30.8\%$ to 0.7%, concluding on the significant improvement of the phase image quality. The associated gains are listed in table 1.

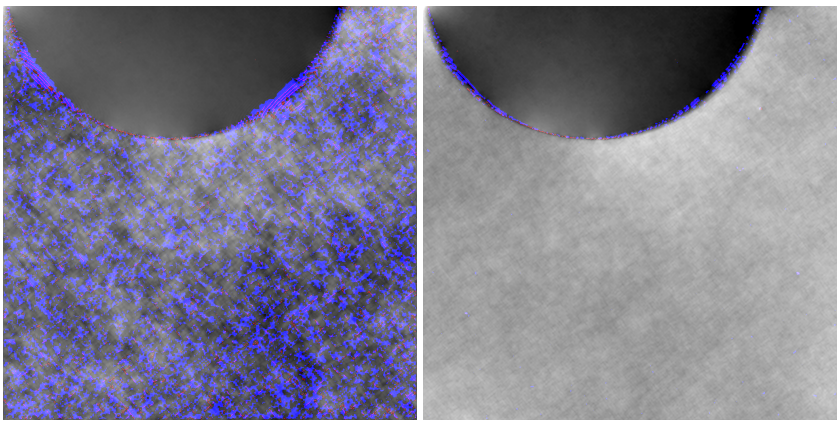

(a) (b)

Fig. 8. (a) CFRP raw phase image (see Figure 7 (c)) superimposed to its associated Confidence Map. The under-sampling alerts ϵ_u are displayed in blue and phase dislocation alerts ϵ_d are displayed in red. (b) CFRP phase image processed by MARIO (see Figure 7 (f)) superimposed to its associated Confidence Map. A clear reduction of the alerts is noticeable (see Table 1).

	Under-sampling alerts ϵ_u (%)	Dislocation alerts ϵ_d (%)
Without MARIO	30.8	3.2
With MARIO	0.7	0.2
Gain	44.0	16.0

Table 1. Table of the Confidence Map values of the CFRP phase image before and after MARIO and associated gains.

5. Conclusion

In this paper, artifacts in phase images have been studied through the Fourier formalism. We have demonstrated that they are mainly related to the extension of the central harmonic which originates from the attenuation and edge intensity overshoot of the object. These additional

frequencies overlap with the modulated harmonics of the grating, making the phase retrieval process less robust. This observation has led to the generation of a preventive computing approach, aiming at removing the parasitic frequencies from the grating ones. We call it *Method of Artifacts Reduction from the Intensity of the Object* (MARIO). We have applied this method in the case of a Carbon Fiber Reinforced Polymer (CFRP) used in the aeronautic field and we have demonstrated quantitatively, thanks to the Confidence Map, that the quality of the phase image could be significantly improved, removing efficiently nearly all artifacts in the image. Even if this results is a heavier process due to the acquisition of an additional image, the significant reduction of artifacts makes it a particularly suitable tool for the non-destructive testing and evaluation field, which is often interested in complex objects with abrupt transitions or high resolution texture.

Fundings. Office National d'Etudes et de Recherches Aérospatiales ; Commissariat à l'Énergie Atomique et aux Énergies Alternatives.

Acknowledgments. The authors thanks the Department of Physics Instrumentation Environment Space (DPHY) and the Department of Materials And Structures (DMAS) from ONERA for the availability of the CFRP-test piece.

Disclosures. The authors declare no conflicts of interest.

Data availability. The data presented in this study are available from the corresponding author on reasonable request.

Supplementary Materials. See supplementary materials *confidence_map_CFRP_without_MARIO.avi* and *confidence_map_CFRP_with_MARIO.avi* for a better visualisation of Figure 8 (a,b) respectively.

References

1. K. S. Morgan, D. M. Paganin, and K. K. Siu, "X-ray phase imaging with a paper analyzer," Appl. Phys. Lett. **100**, 124102 (2012).
2. S. Bérujon, E. Ziegler, R. Cerbino, and L. Peverini, "Two-dimensional x-ray beam phase sensing," Phys. Rev. Lett. **108**, 158102 (2012).
3. A. Momose, S. Kawamoto, I. Koyama, Y. Hamaishi, K. Takai, and Y. Suzuki, "Demonstration of x-ray talbot interferometry," Jpn. J. Appl. Phys. **42**, L866 (2003).
4. T. Weitkamp, A. Diaz, C. David, F. Pfeiffer, M. Stampanoni, P. Cloetens, and E. Ziegler, "X-ray phase imaging with a grating interferometer," Opt. Express **13**, 6296–6304 (2005).
5. F. Pfeiffer, T. Weitkamp, O. Bunk, and C. David, "Phase retrieval and differential phase-contrast imaging with low-brilliance x-ray sources," Nat. Phys. **2**, 258–261 (2006).
6. K. S. Morgan, D. M. Paganin, and K. K. Siu, "Quantitative x-ray phase-contrast imaging using a single grating of comparable pitch to sample feature size," Opt. Lett. **36**, 55–57 (2011).
7. H. H. Wen, E. E. Bennett, R. Kopace, A. F. Stein, and V. Pai, "Single-shot x-ray differential phase-contrast and diffraction imaging using two-dimensional transmission gratings," Opt. Lett. **35**, 1932–1934 (2010).
8. H. Lim, Y. Park, H. Cho, U. Je, D. Hong, C. Park, T. Woo, M. Lee, J. Kim, N. Chung, J. Kim, and J. Kim, "Experimental setup and the system performance for single-grid-based phase-contrast x-ray imaging (pcxi) with a microfocus x-ray tube," Opt. Commun. **348**, 85–89 (2015).
9. S. Tahir, S. Bashir, C. MacDonald, and J. C. Petruccelli, "Mesh-based phase contrast fourier transform imaging," Opt. Commun. **389**, 103–109 (2017).
10. J. Primot, "Three-wave lateral shearing interferometer," Appl. Opt. **32**, 6242–6249 (1993).
11. J. Rizzi, T. Weitkamp, N. Guérineauu, M. Idir, P. Mercère, G. Druart, G. Vincent, P. da Silva, and J. Primot, "Quadriwave lateral shearing interferometry in an achromatic and continuously self-imaging regime for future x-ray phase imaging," Opt. Lett. (2011).
12. J. Rizzi, P. Mercere, M. Idir, P. Da Silva, G. Vincent, and J. Primot, "X-ray phase contrast imaging and noise evaluation using a single phase grating interferometer," Opt. Express **21**, 17340–17351 (2013).
13. P. Podder, T. Z. Khan, M. H. Khan, and M. M. Rahman, "Comparative performance analysis of hamming, hanning and blackman window," Int. J. Comput. Appl. **96** (2014).
14. C. He, W. Sun, C. MacDonald, and J. C. Petruccelli, "The application of harmonic techniques to enhance resolution in mesh-based x-ray phase imaging," J. Appl. Phys. **125**, 233101 (2019).
15. A. Stolidi, G. Giakoumakis, J. Primot, A. Jarnac, and D. Tisseur, "Confidence map tool for gradient-based x-ray phase contrast imaging," Opt. Express **30**, 4302–4311 (2022).
16. M. Takeda, H. Ina, and S. Kobayashi, "Fourier-transform method of fringe-pattern analysis for computer-based topography and interferometry," J. Opt. Soc. Am. (1982).

17. R. S. Martins, C. Zaepffel, F. Tholin, and P. Lalande, “Characterization of dynamic carbon-metallic contact resistance submitted to a lightning current waveform,” presented at international conference on lightning static electricity, Wichita, USA, (10-13 Sept. 2019).